Using stratification to mitigate end-effects in quasi-Keplerian Taylor–Couette flow

Colin Leclercq[1]†, Jamie L. Partridge[2], Pierre Augier[2], Stuart B. Dalziel[2], Rich R. Kerswell[1]

[1]School of Mathematics, University of Bristol, University Walk, Bristol BS8 1TW, United Kingdom

[2]Department of Applied Mathematics and Theoretical Physics, Centre for Mathematical Sciences, Wilberforce Road, Cambridge CB3 0WA, United Kingdom

Efforts to model accretion disks in the laboratory using Taylor–Couette flow apparatus are plagued with problems due to the substantial impact the end-plates have on the flow. We explore the possibility of mitigating the influence of these end-plates by imposing stable stratification in their vicinity. Numerical computations and experiments confirm the effectiveness of this strategy for restoring the axially-homogeneous quasi-Keplerian solution in the unstratified equatorial part of the flow for sufficiently strong stratification and moderate layer thickness. If the rotation ratio is too large, however, (e.g. $\Omega_o/\Omega_i = (r_i/r_o)^{3/2}$ where Ω_o/Ω_i is the angular velocity at the outer/inner boundary and r_i/r_o is the inner/outer radius) the presence of stratification can make the quasi-Keplerian flow susceptible to the stratorotational instability. Otherwise (e.g. for $\Omega_o/\Omega_i = (r_i/r_o)^{1/2}$) our control strategy is successful in reinstating a linearly-stable quasi-Keplerian flow away from the end-plates. Experiments probing the nonlinear stability of this flow show only decay of initial finite-amplitude disturbances at a Reynolds number $Re = O(10^4)$. This observation is consistent with most recent computational (Ostilla-Mónico *et al.* 2014) and experimental results (Edlund & Ji 2014) at high Re, and reinforces the growing consensus that turbulence in cold accretion disks must rely on additional physics beyond that of incompressible hydrodynamics.

Key words:

1. Introduction

In the past decade or so there has been much controversy about transition to turbulence in laboratory experiments of centrifugally-stable Taylor–Couette flow (Balbus 2011). The motivation behind these experiments has been to uncover physical mechanisms to explain the origin of turbulence in accretion disks where, in the simplest model of a non-self-gravitating disk, the angular velocity $\Omega \sim r^{-3/2}$ decreases with radius r while the angular momentum $L = r^2\Omega \sim r^{1/2}$ increases: so-called Keplerian flow. This flow is centrifugally-stable according to Rayleigh's criterion (Rayleigh 1917). The connection with Taylor–Couette flow (Zeldovich 1981) lies in the fact that a similar 'Rayleigh–stable' flow can be set up by appropriate motion of the inner and outer cylinders. Specifically, if we define the ratios $\eta := r_i/r_o$ and $\mu := \Omega_o/\Omega_i$, where the inner (resp. outer) cylinder at $r = r_i$

† Email address for correspondence: c.leclercq@bristol.ac.uk

(resp. $r = r_o$) rotates at Ω_i (resp. Ω_o) – see figure 1 – then the angular velocity in the interior is

$$\Omega_{TC} = \frac{\Omega_i}{1 - \eta^2}\left[\mu - \eta^2 + (1 - \mu)\frac{r_i^2}{r^2}\right] \qquad (1.1)$$

with 'quasi-Keplerian' flows – $\mathrm{d}|\Omega|/\mathrm{d}r < 0$ and $\mathrm{d}|L|/\mathrm{d}r > 0$ – corresponding to the parameter range

$$\eta^2 < \mu < 1. \qquad (1.2)$$

In the presence of an axial magnetic field, quasi-Keplerian Taylor–Couette flow (Velikhov 1959; Chandrasekhar 1960) and accretion disks (Balbus & Hawley 1991, 1998) are known to be prone to the magnetorotational instability. However, this linear instability mechanism cannot operate in weakly ionized accretion disks, which led to the hypothesis (Richard & Zahn 1999) that disk turbulence was the result of a finite-amplitude instability of Keplerian flow. Subsequently, a number of experiments were aimed at assessing this subcritical transition scenario in the laboratory.

Unfortunately, this deceptively simple idea has proven hard to implement in practice (leaving aside the unreachable values of $Re > 10^9$ in accretion disks (Turner *et al.* 2014)) because of significant effects caused by the top and bottom boundaries necessary to contain the fluid. As explained by Czarny *et al.* (2003), the no-slip boundary condition disturbs the balance between the centrifugal force and the radial pressure gradient which prevails in the interior. This force imbalance leads to Ekman layers on the end-plates and, consequently, to a radial flow there, which in turn drives a global meridional circulation. In the centrifugally-stable regime, Avila *et al.* (2008) showed that the two symmetric recirculation cells are able to penetrate deep into the flow and merge at the equator (defined as the plane $z = 0$ in figure 1) to form an unstable radial jet (this will be discussed further in §4.1.1). This experimental artifact clearly compromises the analogy between Taylor–Couette flow and accretion disks and, as a result, various strategies have been implemented to minimise these end-effects. The Princeton group (Ji *et al.* 2006) split their endcaps into two independent rings, creating a piecewise constant angular velocity profile at the top and bottom boundaries, and reported that the flow was 'essentially steady' up to $Re = O(10^6)$. On the other hand, the Maryland group (Paoletti & Lathrop 2011) split the inner cylinder of their large-aspect-ratio apparatus into three parts, sensing the torque only on the central section. Their measurements were in contradiction with Ji *et al.* (2006)'s findings and suggested turbulence at similarly high Reynolds number. Later, Avila (2012) reproduced the experiments numerically and found both setups to be linearly unstable and already turbulent at $Re = O(10^3)$, because of instabilities stemming from the end-plates. The Princeton group (Edlund & Ji 2014) recently reported new experiments on a modified device (one independent ring surrounded by end-plates attached to the inner and outer cylinders) showing that these instabilities could be avoided in a narrow range of operating parameters. Using laser-Doppler-velocimetry, the Princeton authors demonstrated agreement of their velocity profiles with (1.1) and also confirmed stability of the flow with respect to finite amplitude perturbations at $Re = O(10^6)$. Recent numerical results by Ostilla-Mónico *et al.* (2014), based on axially periodic DNS for Re up to $O(10^5)$, also seem to indicate nonlinear stability of quasi-Keplerian flows.

In this work, we propose a new approach directed at reducing end-effects in experiments. Our strategy consists of adding stably-stratified layers near the top and bottom plates while leaving the equatorial part of the flow unstratified, as shown in figure 1. The idea is that the stratified layers should suppress vertical motions and therefore act as 'buffer zones' isolating our hydrodynamic model of an accretion disk at the centre of the cylinder from the undesired flow induced by the end-plates. Of course, this approach is
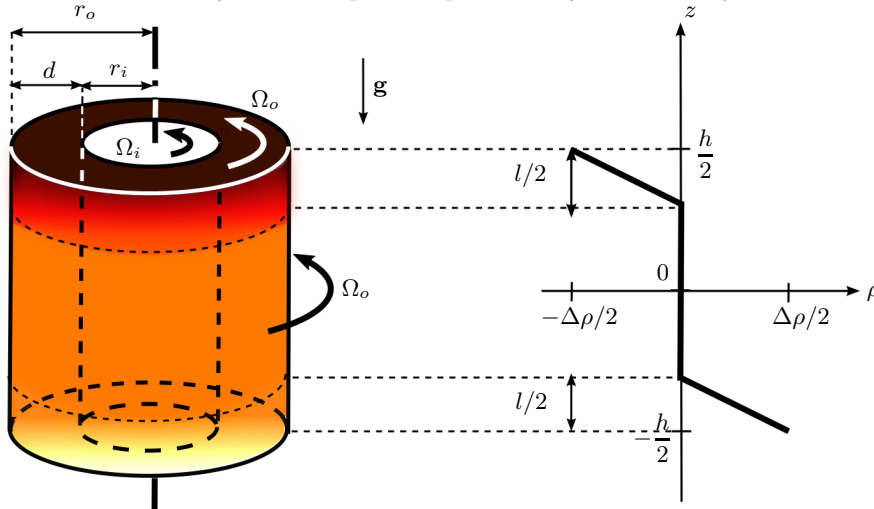
FIGURE 1. Partially stratified Taylor–Couette setup: the flow is linearly stratified in the axial direction z near the end-plates (colour scheme is indicative of temperature). In this paper, the end-plates are attached to the outer cylinder. Rather than the total density, ρ denotes the deviation with respect to a reference value ρ_0.

only useful if stratification does not introduce any linear instabilities into the problem. In the absence of axial boundaries, stratified Taylor–Couette flow is known to be prone to the stratorotational instability (SRI) (so named by Dubrulle *et al.* (2005)) caused by the resonance between boundary-trapped inertia-gravity waves. Originally discovered by Molemaker *et al.* (2001) and Yavneh *et al.* (2001), the instability was theoretically predicted to develop for any value of $\mu < 1$ (cyclonic regime) in the inviscid, small-gap limit. Shalybkov & Rüdiger (2005) and Rüdiger & Shalybkov (2009) later extended these results to the wide gap and viscous case with the help of numerical methods. These authors showed that the instability range was narrower than initially thought, as SRI could only be found for a very limited range of rotation ratios μ beyond η, if at all, depending on the radius ratio and stratification. In parallel, Le Bars & Le Gal (2007) verified their predictions experimentally, providing the first evidence of the existence of SRI. Given the development of SRI in 'fully' stratified flows, the effect of the stratified layers on the global stability of the axisymmetric base flow is systematically assessed in this work.

The plan of the paper is as follows. In §2, we introduce the governing equations of the problem, and then present the numerical and experimental methods in §3. In §4, the effects of stratification 'strength' and layer thickness are assessed for different rotation ratios. In §5, we discuss the physical mechanisms responsible for generation and suppression of meridional flow, the limits of our numerical model, and ultimately the nonlinear stability of the optimally-controlled flow. Finally, section 6 summarizes our main results.

2. Governing equations

The dimensional parameters of the problem are defined in figure 1. There are seven independent non-dimensional parameters specifying the problem. The geometry of the container requires two:

$$\eta := \frac{r_i}{r_o} \quad \text{and} \quad \Gamma := \frac{h}{d}, \tag{2.1}$$

where h and $d := r_o - r_i$ are respectively the height of the cylinders and the radial gap between them. In all computations and experiments, the radius ratio and aspect ratio are set to $\eta = 0.417$ and $\Gamma = 3$ (except for validation, cf. figure 2(b)). The rotation and shear imposed on the fluid are quantified by the Reynolds number and rotation ratio

$$Re := \frac{r_i \Omega_i d}{\nu} \quad \text{and} \quad \mu := \frac{\Omega_o}{\Omega_i}, \tag{2.2}$$

where ν is the kinematic viscosity. The quasi-Keplerian range $\eta^2 < \mu < 1$ is bordered by solid-body rotation (no shear) $\mu = 1$ and the so-called 'Rayleigh line' $\mu = \eta^2$ where the angular momentum is constant over radius. Describing stratification requires three more non-dimensional numbers. Let ρ_{tot} denote the density field and $\rho := \rho_{\text{tot}} - \rho_0$ be the deviation with respect to the reference value $\rho_0 := \rho_{tot}(z = 0, t = 0)$, such that ρ is initially antisymmetric with respect to z. The initial buoyancy frequency within the layers is $N := \sqrt{-(g/\rho_0)\partial\rho/\partial z}$, where g denotes gravity. The strength of the initial stratification is quantified by the *local* Richardson number

$$Ri_l := N^2/\Omega_i^2. \tag{2.3}$$

The ratio of the momentum diffusion coefficient ν to the density diffusion coefficient κ is either the Prandtl number Pr for thermal stratification or the Schmidt number Sc for salt stratification

$$Pr, Sc := \frac{\nu}{\kappa}. \tag{2.4}$$

Momentum and density diffusion time scales across the gap d are given by $\tau_\nu := d^2/\nu$ and $\tau_\kappa := d^2/\kappa$. Finally, the stratified fraction

$$0 \leqslant \alpha := \frac{l}{h} \leqslant 1 \tag{2.5}$$

is defined as the ratio between the thickness $l/2$ of each stratified layer and the half height $h/2$ of the apparatus. With these definitions, the buoyancy frequency can be expressed as $N = \sqrt{g\Delta\rho/(\rho_0\alpha\Gamma d)}$.

The flow is governed by the incompressible Navier–Stokes equations in the Boussinesq approximation, relying on the assumption that $\Delta\rho/\rho_0 \ll 1$ and that curvature of the isopycnals due to centrifugal effects can be neglected. In the following, we choose d, $r_i\Omega_i$ and $\Delta\rho$ as typical length, velocity and density scales in order to obtain non-dimensional quantities. In cylindrical coordinates (r, θ, z), the dynamical equations for the velocity $\mathbf{u} = u\mathbf{e}_r + v\mathbf{e}_\theta + w\mathbf{e}_z$ and density ρ read:

$$\partial_t u + u\partial_r u + \frac{v}{r}\partial_\theta u + w\partial_z u - \frac{v^2}{r} = -\partial_r p + \frac{1}{Re}\left(\nabla^2 u - \frac{u}{r^2} - \frac{2}{r^2}\partial_\theta v\right), \tag{2.6a}$$

$$\partial_t v + u\partial_r v + \frac{v}{r}\partial_\theta v + w\partial_z v + \frac{uv}{r} = -\frac{1}{r}\partial_\theta p + \frac{1}{Re}\left(\nabla^2 v - \frac{v}{r^2} + \frac{2}{r^2}\partial_\theta u\right), \tag{2.6b}$$

$$\partial_t w + u\partial_r w + \frac{v}{r}\partial_\theta w + w\partial_z w = -\partial_z p + \frac{1}{Re}\nabla^2 w - Ri_g\rho, \tag{2.6c}$$

$$\partial_t \rho + u\partial_r \rho + \frac{v}{r}\partial_\theta \rho + w\partial_z \rho = \frac{1}{ReSc}\nabla^2\rho, \tag{2.6d}$$

where

$$\nabla^2 := \partial_{rr}^2 + \frac{1}{r}\partial_r + \frac{1}{r^2}\partial_{\theta\theta}^2 + \partial_{zz}^2 \tag{2.7}$$

is the scalar Laplacian operator, $p := \Pi/\rho_0 + gz$ is a potential based on the pressure Π,

and finally

$$Ri_g := \alpha\Gamma\frac{(1-\eta)^2}{\eta^2}Ri_l \tag{2.8}$$

is a *global* Richardson number (created in the equations by the choice of reference scales).

In strongly rotating flows, 'centrifugal buoyancy' can be taken into account by including the nonlinear term $(\Delta\rho/\rho_0)\rho(\mathbf{u}\cdot\boldsymbol{\nabla})\mathbf{u}$ in the convective derivative (Lopez *et al.* 2013). This term is $O(\Delta\rho/\rho_0)$ with our choice of reference scales, whereas the usual buoyancy term related to gravity is $O(Ri_g)$. In the present study, $Ri_g \gg \Delta\rho/\rho_0$ (see parameter values in table 1), which justifies the use of the traditional Boussinesq approximation. The incompressibility constraint can be written as

$$\partial_r u + \frac{u}{r} + \frac{1}{r}\partial_\theta v + \partial_z w = 0. \tag{2.9}$$

The meridional velocity $\mathbf{u}_\perp := (u, w)$ vanishes at the boundaries whereas the zonal component satisfies

$$v = \begin{cases} 1 & \text{if } r = r_i^\star, \; |z| \leqslant \Gamma/2, \\ \mu/\eta & \text{if } r = r_o^\star, \; |z| \leqslant \Gamma/2, \\ \mu(r/r_i^\star) & \text{if } r_i^\star < r \leqslant r_o^\star, \; |z| = \Gamma/2, \end{cases} \tag{2.10}$$

where $r_i^\star = \eta/(1-\eta)$ and $r_o^\star = 1/(1-\eta)$ denote respectively the nondimensional inner and outer radii. Finally, we impose the piecewise-linear density profile

$$\rho = \begin{cases} -\dfrac{1}{2\alpha}\left[\dfrac{2z}{\Gamma} - (1-\alpha)\right] & \text{if } 1-\alpha \leqslant 2z/\Gamma \leqslant 1, \\ -\dfrac{1}{2\alpha}\left[\dfrac{2z}{\Gamma} + (1-\alpha)\right] & \text{if } 1-\alpha \leqslant -2z/\Gamma \leqslant 1, \\ 0 & \text{otherwise.} \end{cases} \tag{2.11}$$

either initially in the volume in the case of salt stratification, or at the boundaries at all times in the case of temperature stratification. Indeed, in the former case, the density satisfies no-flux (Neumann) boundary conditions at the walls $\partial_n\rho = 0$ (where ∂_n denotes the wall-normal derivative), whereas in the latter case, the temperature on the walls can be controlled such that (2.11) holds for all time there (Dirichlet boundary conditions).

3. Methods

3.1. *Numerical methods*

In the following, the flow variables are jointly written as $\mathbf{q} := (\mathbf{u}, p, \rho)$. Base flow quantities are denoted with capital letters or subscript 'B' for Greek characters, hence $\mathbf{Q} = (\mathbf{U}, P, \rho_B)$. Perturbations with respect to the base flow are denoted $\mathbf{q}' := \mathbf{q} - \mathbf{Q}$.

3.1.1. *Temperature stratification: steady base flows*

In the case of temperature stratification, the base flow is steady, axisymmetric and has the z-symmetry

$$\mathcal{Z} : (U, V, W, P, \rho_B)(r, z) \rightarrow (U, V, -W, P, -\rho_B)(r, -z) \tag{3.1}$$
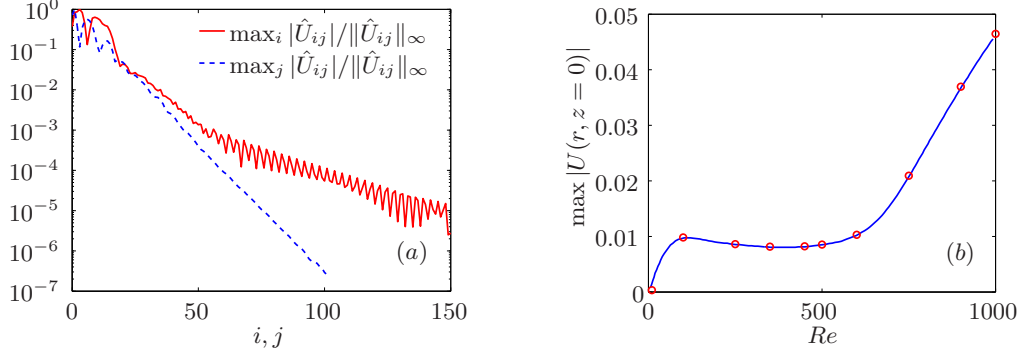
FIGURE 2. (a) Convergence of spectral coefficients $\hat{U}_{ij}$ of the radial velocity component, for $\mu = \eta^{1/2}$, $\alpha = 0.5$ and $Ri_l = 2$. (b) Maximum radial velocity at the equator for $\eta = 0.5$, $\Gamma = 6$, $\mu = 1$, fixed end-plates and no stratification. Solid line: data digitized from Avila *et al.* (2008), dots: present code.

as a consequence of the Boussinesq approximation and the imposed boundary conditions. Each field was discretized using a double expansion of Chebyshev polynomials,

$$Q(r, z) = \sum_{i=0, j=0}^{I, J} \hat{Q}_{ij} T_i \left(2(r - r_i^\star) - 1\right) \Phi_j \left(2z/\Gamma\right) \qquad (3.2)$$

where $T_i(x) := \cos(i \cos^{-1} x)$ and $\Phi_j(x) := T_{2j}(x)$ or $T_{2j+1}(x)$, depending on whether the field Q is symmetric or antisymmetric in z. Because of the absence of boundary conditions on P, the corresponding expansion (3.2) was truncated at order $(I - 2, J - 1)$ instead of (I, J) in this case (see Peyret (2002)). The governing equations were solved directly in the physical space using a collocation method. Discontinuities in (2.10) (at $r = r_i^\star$ for $|2z/\Gamma| = 1$) and (2.11) (at $|2z/\Gamma| = 1 - \alpha$) were smoothed in order to preserve spectral accuracy. This was achieved by introducing a small length scale δ, following Lopez & Shen (1998), and defining new boundary conditions for the azimuthal velocity

$$V = \frac{r}{r_i^\star} \left[\mu + (1 - \mu) \exp\left(-\frac{r - r_i^\star}{\delta}\right)\right], \qquad (3.3)$$

and density ρ_B, by integration of

$$\partial_z \rho_B = -\frac{1}{2\alpha\Gamma} \left[2 + \tanh\left(\frac{z - \Gamma/2(1 - \alpha)}{\delta}\right) - \tanh\left(\frac{z + \Gamma/2(1 - \alpha)}{\delta}\right)\right] \qquad (3.4)$$

with respect to z. A value of $\delta = 0.006$ was taken for the computations, following Avila *et al.* (2008). Solutions were computed by Newton–Raphson iteration until the residuals $\|Q^{n+1} - Q^n\|_\infty / \|Q^n\|_\infty$ converged below 10^{-8} for each component Q of $\mathbf{Q}$. All base flow computations were performed with $(I, J) = (101, 150)$, ensuring that the trailing coefficients were always between 4 and 5 orders of magnitude lower than the maximum coefficient. Figure 2(a) shows a typical 'spectral' convergence of the coefficients of (3.2). The solver was also validated against results from Avila *et al.* (2008) (see figure 2(b)) and Abshagen *et al.* (2010).

3.1.2. *Linear stability*

We investigated the linear stability of the base flows computed using temperature boundary conditions. As $\mathbf{Q}$ is steady and axisymmetric, infinitesimal perturbations can be expressed as a superposition of normal modes of the form $\mathbf{q}' = \tilde{\mathbf{q}}'(r, z) \exp[i(m\theta - \omega t)]$,

with azimuthal mode number m and complex frequency ω. These modes either share the z-symmetry (3.1) of the base flow, so that $\mathcal{Z}\mathbf{q}' = \mathbf{q}'$, or are antisymmetric under the action of $\mathcal{Z}$: $\mathcal{Z}\mathbf{q}' = -\mathbf{q}'$. Substituting the normal mode form into the Navier–Stokes equations (2.6)–(2.11) linearized about $\mathbf{Q}$ leads to a generalized eigenvalue problem in ω and $\mathbf{q}'$. Following Leclercq *et al.* (2013), this problem was reduced to a much smaller standard eigenvalue problem by eliminating the pressure, boundary points, and one velocity component ($\tilde{w}'$ if $m = 0$ and $\tilde{v}'$ otherwise) and then solved using standard LAPACK and ARPACK++ routines. The solver was validated against figure 6 of Avila *et al.* (2008) with perfect agreement between our computed values of critical Re and values digitized from the plot for $\Gamma = 3, 4, 6$ and the various m shown.

3.1.3. *Salt stratification: quasi-steady base flows*

In the case of salt stratification, the no-flux boundary conditions lead to a very slow relaxation of the density field to an eventually unstratified state. The time scale of density diffusion τ_κ is larger than 5 months in our apparatus, however, so that the laboratory experiments are quasi-steady after a few momentum diffusion times ($\tau_\nu \sim 5\text{h}30$). The resulting time-dependent base flow is also axisymmetric and invariant under the action of $\mathcal{Z}$. In order to compute these solutions, a time-stepper was developed with no-flux boundary conditions on the density $\partial_n \rho_B = 0$, as in the experiments. The flow was taken initially at rest with a stratification profile given by (3.4) at any radial position. The cylinders and end-plates were then accelerated to their final rotation speed over a few periods $\tau = 0.05\tau_\nu$, by multiplying the boundary condition (3.3) by the factor $(1 - \exp[-t/\tau])$. A streamfunction-vorticity formulation was used and spectral expansions of the form given in (3.2) were again used to discretize the problem (see Peyret (2002), pp. 188–195). Nonlinear terms were treated explicitly with a second-order extrapolation (Adams–Bashforth) whereas the diffusion terms were treated implicitly (backward differentiation). Incompressibility was enforced with an influence matrix. Helmholtz and Poisson problems were solved using a full diagonalization method. The code was validated by applying Dirichlet boundary conditions (3.4) on the density and checking consistency with solutions given by the Newton–Raphson solver.

3.2. *Experimental methods*

Experiments were conducted in a Taylor–Couette tank of height 50 cm with $(r_i, r_o) = (10, 24)$ cm resulting in a radius ratio $\eta = 0.417$. The tank was filled to a depth $h = 42 \pm 2$ cm, giving an aspect ratio $\Gamma = 3 \pm 0.14$. The top and bottom boundaries both rotated with the outer cylinder. A transparent perspex lid, placed in contact with the fluid in the annulus, was fixed to the outer cylinder after filling and formed the top endplate, while the bottom end-plate was securely attached to the rotating table forming the base of the tank. The inner cylinder was driven independently from above by a mounted motor unit, at its maximum rotation rate $\Omega_i = 1 \pm 0.03$ rad s^{-1} for all experiments. The rotation rate Ω_o of the rotating table was varied to achieve the desired value of μ.

The experiments began by filling the tank to the desired stratification using two computer-controlled peristaltic pumps. The two pumps were connected to different reservoirs of fluid, one of relatively dense NaCl solution and the other of fresh water, both of which had been de-aerated using vacuum cylinders to reduce unwanted air coming out of the solution during the course of an experiment and hindering the visualisation. The reservoirs also sat out for approximately one day to equilibrate with the ambient temperature conditions of the laboratory. The density of the two reservoirs were measured just prior to filling using an Anton Paar DMA5000 density meter with a resolution of 10^{-6} g cm^{-3}. After filling, a conductivity probe was then traversed through the depth of

the tank to measure the resulting stratification. Due to the long filling time ($\sim 1-2$ hours), the flow rates in the pumps could deviate during the filling procedure resulting in a small error of the desired fill height ($\pm 5\%$). We do not expect this small change in aspect ratio to alter the overall flow patterns observed.

To reduce the impact of any initial transient, the cylinders were slowly ramped up over 8 hours ($\sim 1.5\,\tau_\nu$), with the rotation ratio μ held constant during the course of the ramp. After the initial ramp period, the cylinders' rotation rates were held constant for another momentum diffusion time before acquiring any raw images for PIV. After the raw images had been acquired, the cylinders were both ramped down to rest over a momentum diffusion time to minimise unwanted shear before taking a final density profile using the conductivity probe.

To monitor the behaviour of the stratified layers, shadowgraph images were automatically recorded at 30 minute intervals during the experiment. To enable simultaneous capture of PIV and shadowgraph images, the inner cylinder was painted white except for a black band that spanned $z = -9\,\mathrm{cm}$ to $z = 10\,\mathrm{cm}$. A slide projector positioned approximately 3 m from the tank illuminated the flow and projected refractive index variations onto the white regions of the inner cylinder, which were then recorded using a Uniq Vision UP1830-12B 1 MPixel resolution camera.

Raw images for PIV were captured using a 4 MPixel Dalsa Falcon 2 camera at 160 fps for 30 seconds (~ 5 rotation periods of the inner cylinder). The camera was mounted directly above the apparatus, viewing down through the top transparent end-plate. The flow was seeded using $20\,\mu\mathrm{m}$ diameter polyamid particles and illuminated using a 700 W arc lamp. The resulting light sheet was approximately 3 mm thick and was horizontally orientated so all velocity data are in the (r, θ) plane. For all the data reported here, the light sheet was positioned at $z = 0 \pm 1\,\mathrm{cm}$ so data are acquired in the centre of the unstratified region. The region illuminated and captured by the camera was 14 cm $\times$ 3 cm which corresponded to 1800 pixels $\times$ 400 pixels. Particle image velocimetry was analysed using DigiFlow (Dalziel *et al.* 2007) with an interrogation window size 32 pixels $\times$ 32 pixels and an overlap of 50% that results in a spatial resolution of $\sim 1.24\,\mathrm{mm}$. The error in particle displacements was ~ 0.02 of a pixel which gives an error in velocity of $\sim 0.25\,\mathrm{mm\,s^{-1}}$ ($\sim 0.025\%$ of $r_i\Omega_i$).

4. Mitigating end-effects with stratification

Table 1 summarizes the values of the different control parameters taken in our experiments and computations. Two rotation ratios were considered in both: a 'high-shear' (HS) value where $\mu = \eta^{3/2}$ and a 'low-shear' (LS) one where $\mu = \eta^{1/2}$. We recall that the quasi-Keplerian range is $\eta^2 < \mu < 1$ with the upper limit $\mu = 1$ corresponding to uniform rotation and therefore *no* shear. Here we use the terms 'low' and 'high' only to distinguish the two cases by comparison with one another, but note that arbitrarily large shear rates can be achieved even in the LS case, by setting Re to a large enough value.

Because of our underlying objective of investigating the existence of turbulence in quasi-Keplerian flow, we indeed chose to maximise the value of the Reynolds number in the experiments, leading to $Re = 14000$ with our set-up. However, accurate computations could not be achieved at this large value of Re in a reasonable time frame with our serial codes, so an upper limit of $Re = 5000$ was taken for these.

Salt was used to generate stratification in the experiments, so the density field satisfied no-flux boundary conditions at the walls and the Schmidt number was $Sc \approx 700$. However, for reasons which will be discussed further in §5.3, we chose to model the experiment with Dirichlet boundary conditions at the walls, instead of Neumann conditions.

parameters		simulations	experiments
geometry	η	0.417	0.417
	Γ	3	3 ± 0.14
rotation and shear	Re	5000	14000 ± 700
	μ	$\eta^{1/2}$ (LS), $\eta^{3/2}$ (HS)	
stratification	Ri_l	$0 - 5$	$0, 2$
	α	$0 - 1$	$0, 0.5, 1$
	Sc or Pr	$Pr = 7$	$Sc \approx 700$
	B.C. on ρ	Dirichlet	Neumann

TABLE 1. Comparison between numerical and experimental control parameters. For the stratified experiment with $\alpha = 0.5$, $Ri_l = 2$, and the larger value of $Re = 14000$, $Ri_g \approx 6$ and $\Delta\rho/\rho_0 \approx 0.04$ so the condition $Ri_g \gg \Delta\rho/\rho_0$ is well-satisfied. 'Centrifugal buoyancy' is therefore expected to be negligible compared to 'gravitational buoyancy', justifying the use of the Boussinesq approximation.

In practice, this would correspond to imposing a temperature profile at the walls, which would lead to much quicker density diffusion, as heat diffuses more rapidly than salt in fresh water ($Pr \approx 7$ instead of $Sc \approx 700$). This other discrepancy will be discussed in §5.2. Put simply, these modelling choices for stratification made our equations much more amenable to numerical computation than if actual experimental settings were taken.

The computed meridional and zonal base flows are presented in figures 3 and 4 for the two shear cases and three choices of stratification: no stratification ($\alpha = 0$), full stratification ($\alpha = 1$) and partial stratification ($0 < \alpha < 1$). Each case is discussed in more detail in the following subsections.

4.1. *Unstratified case: $\alpha = 0$*

4.1.1. *'High-shear case' $\mu = \eta^{3/2}$*

In the absence of stratification, the meridional circulation for the HS case penetrates deep into the flow and causes a strong distortion of the azimuthal flow field, as can be seen in figure 3(a). The driving mechanism is a broken balance between centrifugal force and pressure gradient at the end-plates caused by the no-slip boundary condition (Czarny *et al.* 2003). The inward radial flow at the endcaps is then redirected to the equatorial region through Stewartson layers once it reaches the inner cylinder. This leads to the formation of two meridional recirculation cells that merge at the equator into a strong outward radial jet (Avila *et al.* 2008). The jet redistributes angular momentum along r, leading to a locally centrifugally unstable angular momentum profile, i.e. $d|L|/dr < 0$ for $0 \lesssim r - r_i^\star \lesssim 0.63$ and $z = 0$. The structure of the resulting global mode linear instability is represented in figure 5(a). In the experiment, this instability develops into turbulent motion, characterised by high levels of velocity fluctuations in the equatorial plane: $\sqrt{\overline{\delta u^2 + \delta v^2}}/\overline{v}$ up to $5 - 6\%$ near the inner cylinder ($\overline{(.)}$ denotes temporal average and $\delta\mathbf{u}$ is the fluctuation with respect to the mean: $\delta\mathbf{u} := \mathbf{u} - \overline{\mathbf{u}}$), as shown by the dashed line in figure 6. Turbulence tends to homogenise angular momentum in centrifugally-unstable regions, explaining the deviation between the computed base flow (dashed line) and the time-averaged azimuthal velocity (solid line with markers) for $0 \lesssim r - r_i^\star \lesssim 0.7$ in figure 7(a).
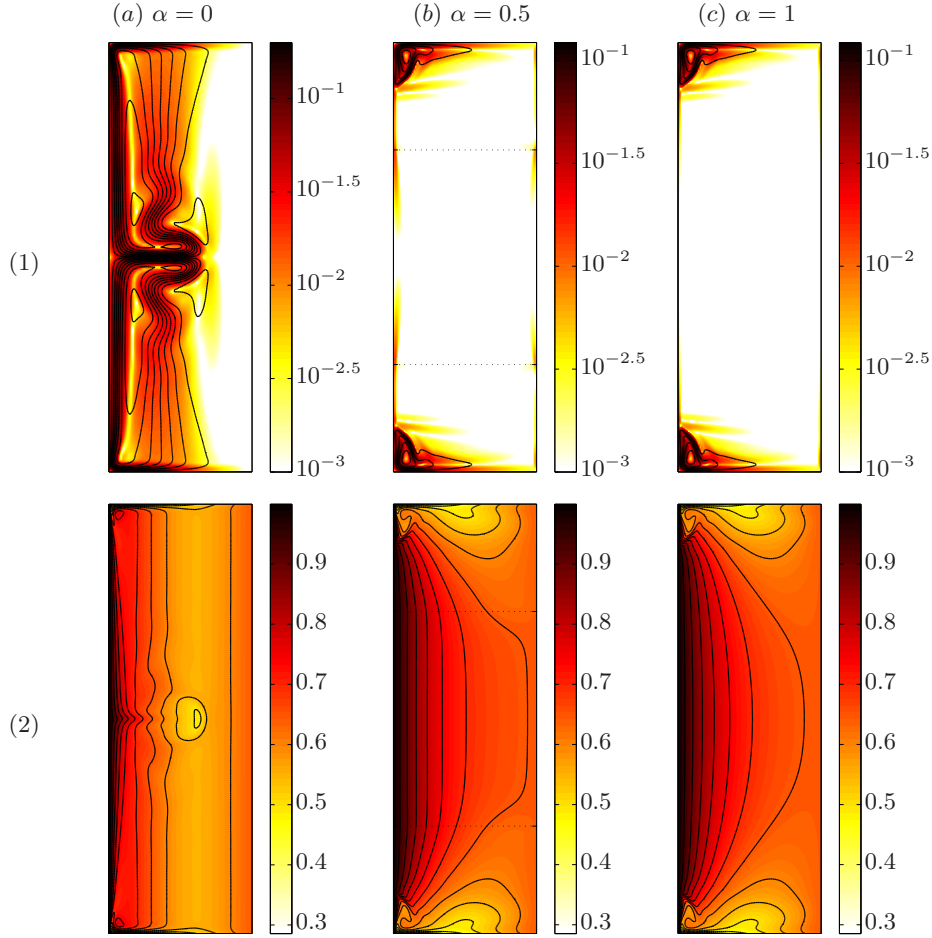
FIGURE 3. Base flow for the HS case $\mu = \eta^{3/2}$ (1) Meridional flow $\mathbf{U}_\perp = (U, W)$: streamlines $(\Delta\psi = 10^{-3})$ and colourmap of the norm $\|\mathbf{U}_\perp\|$. (2) Azimuthal velocity V: colourmap and contours of V ($\Delta V = 0.05$). Dotted lines in (b) indicate the limit of the stratified layers. In this figure and hereafter, the left (resp. right) boundary corresponds to the inner (resp. outer) cylinder.

4.1.2. *'Low-shear case'* $\mu = \eta^{1/2}$

Although the end-plates generate large scale meridional circulation in the LS case, the symmetric cells in figure 4(1a) do not appear to reach the equator. As a result, the axial homogeneity of the zonal flow V is preserved across $z = 0$ and the flow is numerically found to be linearly stable. Correlatively, velocity fluctuations in the experiments remain small with $\sqrt{\delta u^2 + \delta v^2}/\overline{v} \sim 1\%$ at the equator (solid line in figure 6). In fact, apart from rapid variations in boundary layers near the end-plates, the azimuthal velocity seems virtually independent of z across the entire container. However, a closer look at the radial profile of $\overline{v}$ in figure 7(b) shows significant differences between the experiments (solid line with markers) and the ideal Taylor–Couette solution (thick solid line). This mismatch can be interpreted as a manifestation of the Taylor–Proudman theorem in rapidly rotating flows, as explained in Hollerbach & Fournier (2004). Indeed, in the LS case, the Rossby number (defined as in Hollerbach & Fournier (2004) and Paoletti & Lathrop (2011)) $Ro := (\Omega_i - \Omega_o)/\Omega_o = (1 - \mu)/\mu$ is small ($Ro \approx 0.55$ for $\eta = 0.417$) and

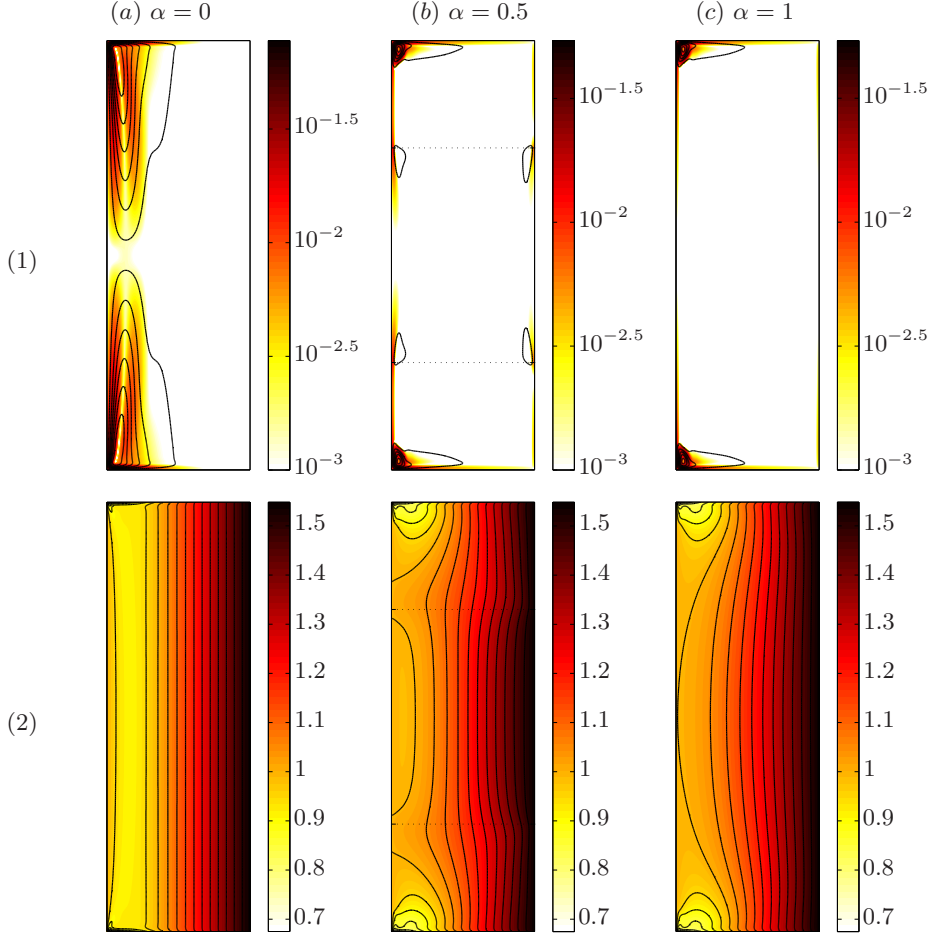(a) $\alpha = 0$ (b) $\alpha = 0.5$ (c) $\alpha = 1$

FIGURE 4. Base flow in the LS case $\mu = \eta^{1/2}$. Same caption as figure 3, except that here $\Delta\psi = 2.5 \times 10^{-4}$.

the flow is not very far from geostrophic balance. It is therefore nearly invariant along the axial direction and controlled by Ekman pumping at the end-plates. Thus, despite weak meridional circulation and stability, experiments in the LS case do not yield the desired Taylor–Couette solution (1.1).

4.2. *Fully stratified case: $\alpha = 1$*

In this section, we investigate the effect of stratification across the entire container. The choice of $Ri_l = 2$ in figures 3(c), 4(c) and 5(c) will be justified later in §4.3.

4.2.1. *'High-shear case' $\mu = \eta^{3/2}$*

The addition of stratification in our axisymmetric computations results in a dramatic reduction in meridional circulation and subsequent zonal flow distortion for the HS case as can be seen in figure 3(1c). Apart from boundary layers at the end-plates and a small 'eddy' trapped in the inner corners, the magnitude of $\mathbf{U}_\perp$ has dropped to less than 0.1% of the inner cylinder velocity everywhere in the flow. As a result, the azimuthal flow now weakly depends on z in the equatorial region and solution (1.1) (thick solid red line) is
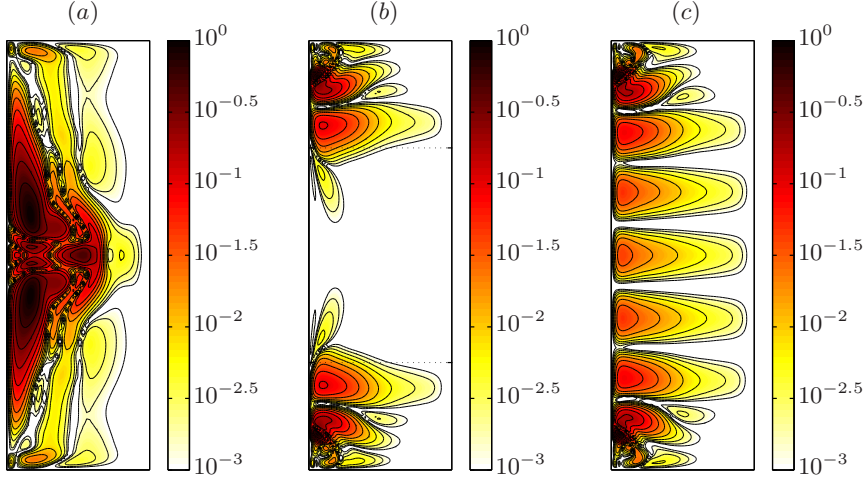
FIGURE 5. Structure of the most unstable linear mode for $\mu = \eta^{3/2}$, $Re = 1500$ and (a) $\alpha = 0$ ($m = 2$, symmetric under $\mathcal{Z}$), (b) $\alpha = 0.5$ ($m = 1$, antisymmetric under $\mathcal{Z}$), (c) $\alpha = 1$ ($m = 1$, symmetric under $\mathcal{Z}$). The production of perturbation energy (kinetic + potential) over the volume $\mathcal{V}$ of the container can be expressed as $\mathcal{P}_\mathcal{V} = - \int_\mathcal{V} \mathbf{u}' \cdot \boldsymbol{\nabla}\mathbf{U} \cdot \mathbf{u}' \mathrm{d}\mathcal{V}$. We introduce the density $\widetilde{\mathcal{P}}(r, z)$ by writing $\mathcal{P}_\mathcal{V}$ as $4\pi \mathrm{e}^{\mathrm{i}2\omega_\mathrm{i}t} \int \widetilde{\mathcal{P}}(r, z) r \mathrm{d}r \mathrm{d}z$. The quantity $r\widetilde{\mathcal{P}}(r, z)$ indicates the distribution of positive production of perturbation energy in the meridional plane, averaged over θ. Contour lines: $\Delta \log_{10}\left[r\widetilde{\mathcal{P}}(r, z)\right] = 0.25$. Dotted lines in (b) mark the limits of the stratified layers. The resolution here is $(I, J) = (67, 100)$.
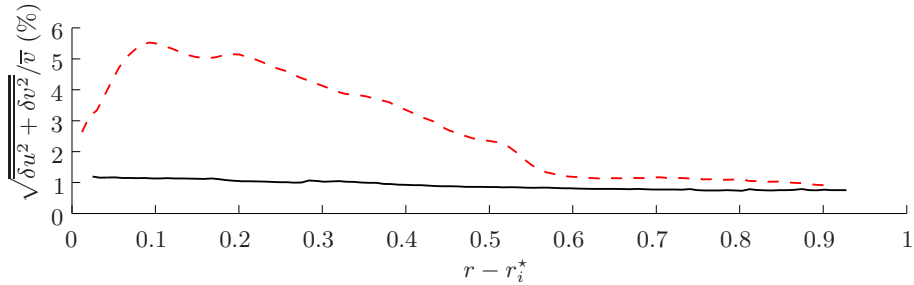

FIGURE 6. PIV measurements of horizontal turbulence intensity at the equator, in the absence of stratification. Comparison between the HS case (dashed red line) and the LS case (solid black line).

almost perfectly recovered at $z = 0$, as can be seen in figure 7(a) (dashed-dotted blue line).

However, despite the fully stratified solutions being significantly closer to the base flow, the computed axisymmetric solution cannot actually be observed in an experiment as the flow is, again, subject to a linear instability. The structure of the most unstable mode, shown for $Re = 1500$ in figure 5(c)), is clearly reminiscent of the SRI as described in Shalybkov & Rüdiger (2005) and Rüdiger & Shalybkov (2009): the mode is non-axisymmetric and almost axially periodic, with an axial wavelength smaller than the gap (for infinite cylinders, Shalybkov & Rüdiger (2005) found the scaling $\lambda \sim Ri_l^{-1/2}$ for the critical axial wavelength λ). However, the production of total disturbance energy is localised near the inner cylinder, which suggests that the instability mechanism for our wide-gap configuration $\eta = 0.417$ is closer to the radiative mechanism of Le Dizès &
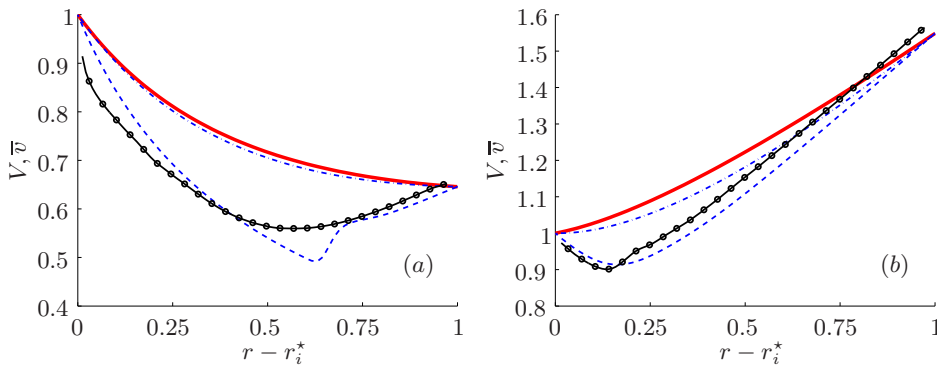
FIGURE 7. Azimuthal velocity profiles at the equator for the (a) HS and (b) LS cases. Solid red lines: axially-invariant Taylor–Couette solution (1.1), dashed blue lines: computed values in the unstratified case, dashed-dotted blue lines: computed base flows in the fully stratified case $(\alpha, Ri_l) = (1, 2)$. Solid black line with markers: time-averaged profiles in the unstratified case, from PIV measurements. There is a small discrepancy in the measured velocity profile due to experimental error ($<5\%$) in setting the rotation rate of the cylinders.

Riedinger (2010) for $\eta \to 0$ than to a resonance between boundary-trapped inertia-gravity waves as discussed by Molemaker *et al.* (2001) in the limit $\eta \to 1$.

4.2.2. *'Low-shear case'* $\mu = \eta^{1/2}$

In the LS case, the effect of stratification on the base flow is similarly beneficial: the meridional flow is negligible except in boundary layers, and the azimuthal velocity is not only almost axially invariant, but also very close to the theoretical solution (1.1) (see figure 7(b); dashed-dotted blue line for the base flow and thick solid red line for the Taylor–Couette solution).

However, a crucial difference with the HS case is that the base flow now remains stable. This is consistent with the predictions of Shalybkov & Rüdiger (2005) and Rüdiger & Shalybkov (2009), who showed that stratified Taylor–Couette flow between infinite cylinders is generally stable for $\mu < \eta$. For the HS case, the presence of end-plates does not seem to impact the structure of the mode far from the end-plates (see 5(c)). Therefore, it may not be surprising to obtain good agreement with theoretical results obtained for an axially invariant base flow in the LS case too.

4.3. *Partially-stratified case:* $0 < \alpha < 1$

The promising numerical results of section §4.2 indicate that stratification is quite powerful at suppressing large meridional circulation cells, which in turn leads to azimuthal velocity profiles close to (1.1). But the end goal of our investigation is to probe the possibility of purely hydrodynamic turbulence, so the central portion of the apparatus needs to be left unstratified and avoid contamination by the stratorotational instability.

Our control strategy hence relies on two parameters: the stratified fraction α and the local Richardson number Ri_l. The effect of these two parameters on the departure of computed solutions with respect to (1.1) is shown in figure 8, in the LS case (results are qualitatively similar for HS). The relative difference between computed and ideal solutions is averaged over a volume spanning half of the unstratified region and centered about the equator. More specifically, we introduce zonal and meridional deviations,

$$\Delta_V := \langle (V - V_{TC})/V_{TC} \rangle_\mathcal{V} \quad \text{and} \quad \Delta_\perp := \langle \|\mathbf{U}_\perp\|/V_{TC} \rangle_\mathcal{V} \tag{4.1}$$
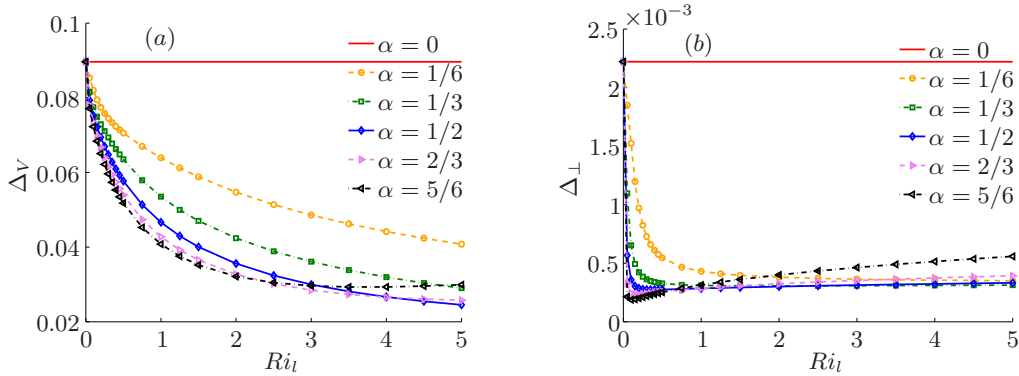
FIGURE 8. (a) Relative azimuthal deviation Δ_V and (b) relative meridional deviation $\Delta_\perp$ as functions of Ri_l, for various values of α, in the LS case.

where $V_{TC} := r\Omega_{TC}$,

$$\langle(.)\rangle_\mathcal{V} := \left(\frac{1}{\mathcal{V}}\int_\mathcal{V}(.)^2\mathrm{d}\mathcal{V}\right)^{1/2} \tag{4.2}$$

and

$$\mathcal{V} := \left\{(r,\theta,z) \in [r_i^\star, r_o^\star] \times [0, 2\pi[\times\left[-\frac{\Gamma(1-\alpha)}{4}, \frac{\Gamma(1-\alpha)}{4}\right]\right\}. \tag{4.3}$$

It appears that both quantities decrease rapidly as Ri_l increases in the range $0 < Ri_l \leqslant 5$. The meridional deviation $\Delta_\perp$ even drops by nearly one order of magnitude within the range $0 < Ri_l < 1$. Increasing Ri_l further has virtually no effect on $\mathbf{U}_\perp$ but keeps improving V. Similarly, the thickness of the layers does not seem critical to the suppression of the meridional flow, as long as $Ri_l \gtrsim 1$. However, thick layers are more efficient at correcting the azimuthal velocity profile, as long as the unstratified zone does not become shallow. Indeed, when $\alpha \geqslant 5/6$, the depth of the unstratified zone becomes lower than half the gap width and the flow in no longer axially homogeneous in this region. This has a negative impact on the deviations, which start increasing again with α and Ri_l.

In this section, we choose to study the case $(\alpha, Ri_l) = (0.5, 2)$, which appears to be a good compromise for various reasons: deviations Δ_V and $\Delta_\perp$ are both small, the aspect ratio of the unstratified zone $\Gamma(1-\alpha) = 1.5$ is larger than 1, and finally this combination is easily achieved experimentally since $\Delta\rho/\rho_0 \approx 4\%$ for $Re = 14000$. This justifies *a posteriori* the choice of $Ri_l = 2$ to illustrate the fully stratified case in §4.2. The density field corresponding to this parameter combination is shown in figure 9 for the HS and LS cases. In both, the isopycnals are almost horizontal, indicating that stratification is 'strong enough' to avoid overturning by the meridional circulation, except at the inner corners (more details will be provided in §5.1).

4.3.1. *'High-shear case'* $\mu = \eta^{3/2}$

There is barely any noticeable difference between the computed meridional flow fields in the fully and partially stratified cases in figure 3(1b & 1c). Apart from boundary layers in the unstratified region for $\alpha = 0.5$, the two fields are almost indistinguishable, confirming that partial stratification efficiently suppresses $\mathbf{U}_\perp$ even when $\alpha \neq 1$. The azimuthal velocity is also remarkably homogeneous along the axial direction in the unstratified zone, but unfortunately, the computed base flow is linearly unstable. The production of energy of the most unstable mode, displayed in figure 5(b) for $Re = 1500$, is precisely localized within the stratified layers. Moreover, the distribution of this quantity is very
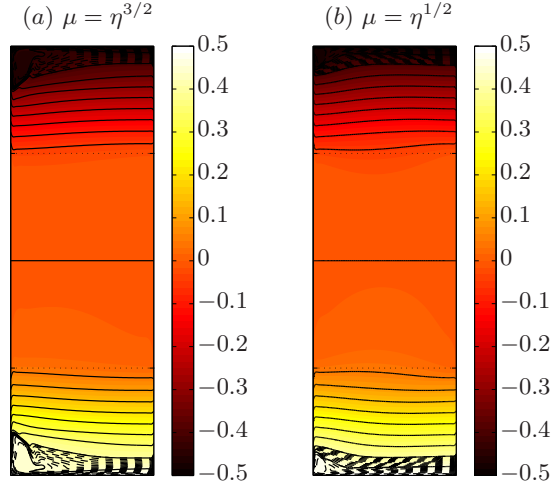
(a) $\mu = \eta^{3/2}$ (b) $\mu = \eta^{1/2}$

FIGURE 9. Base flow density field ρ_B in (a) HS case (unstable) and (b) LS case (stable); $(\alpha, Ri_l) = (0.5, 2)$. Dotted lines mark the limits of the stratified layers. Density step between solid lines: 0.05; between dashed lines: 5×10^{-3}.
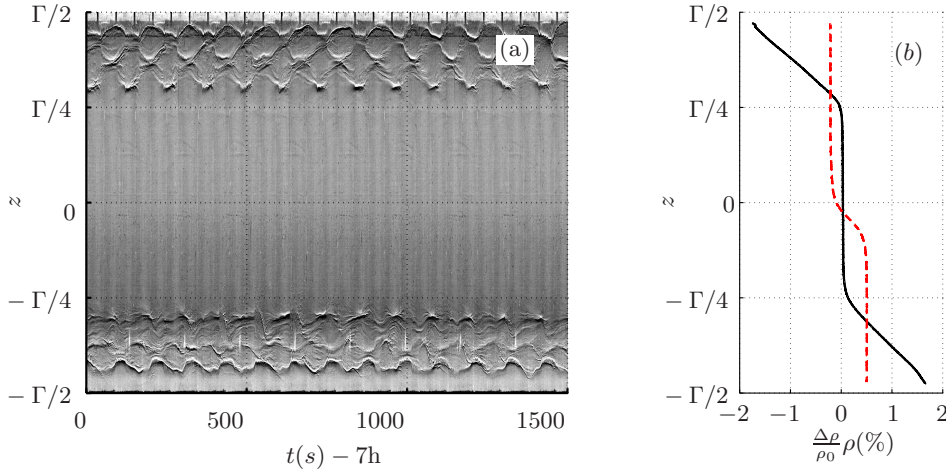

FIGURE 10. Instability of the stratified layers in the HS case with $(\alpha, Ri_l) = (0.5, 2)$. (a) Spatio-temporal diagram of shadowgraph. (b) Density profiles (deviation with respect to the mean ρ_0, nondimensionalised by ρ_0), at mid-gap $r = 1/2(r_i^\star + r_o^\star)$ from conductivity measurements, at $t = 0$ (solid line) and $t = 40\,\mathrm{h}$ (dashed line): the SRI destroys the initial density profile in a few diffusion time units.

similar to that of the fully stratified flow in the same region. Therefore, we conclude that the mode is subject to a stratorotational instability mode localized inside the layers.

Experimentally, this instability leads to the braid pattern visible in the spatiotemporal shadowgraph of figure 10(a). This pattern corresponds to the nonlinear interaction of two helical modes of opposite 'handedness', which are destabilized simultaneously because of symmetry. In the long-term, this secondary flow generates mixing and destroys the initial density profile, as can be seen in figure 10(b).

4.3.2. *'Low-shear case'* $\mu = \eta^{1/2}$

The effect of partial stratification on the base flow in the LS case is similar to that observed for the HS case. The meridional flow is suppressed in the unstratified zone,
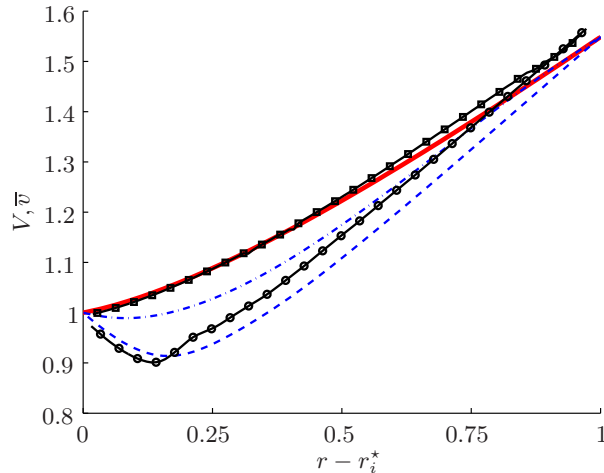
FIGURE 11. Comparison between azimuthal velocity profile at the equator with and without control in the LS case. Thick solid red line – ideal Taylor–Couette solution (1.1). Solid black line with markers – time-averages from experiments (circles – unstratified; squares – partially strati-fied $(\alpha, Ri_l) = (0.5, 2)$). Blue dashed/dashed-dotted lines – computed base flows for unstratified case/partially-stratified case $(\alpha, Ri_l) = (0.5, 2)$. Additional measurements at $z \approx \Gamma/6(1 - \alpha)$ in the partially-stratified case yielded a mean velocity profile nearly indistinguishable from that at $z \approx 0$, hence very close to ideality too. This confirms the effectiveness of the control strategy across a large portion of the volume bounded by the stratified layers.

including within the boundary layer running along the inner cylinder, as $|z| \to 0$. The azimuthal velocity is virtually axially homogeneous in the unstratified region, but con-trary to the unstratified case, the radial profile now closely matches the ideal solution (1.1), as illustrated in figure 11.

For LS, no instability is found (numerically tested up to $Re = 5000$ and experimentally up to 14000) in both the fully and the partially stratified cases. This result is consistent with the analysis of Rüdiger & Shalybkov (2009) who always found linear stability at $\mu = \eta^{1/2}$ (these authors investigated the range $0.3 \leqslant \eta \leqslant 0.78$ and $0.2 \leqslant Ri_l \leqslant 4$).

In conclusion, it appears that the partially-stratified LS case $(\alpha, Ri_l) = (0.5, 2)$ cor-responds to a 'sweet-spot' where stratification efficiently mitigates end-effects without introducing any additional instability mechanism. It is also a realistic set of parameters for an experiment since it only requires $\Delta\rho/\rho_0 \approx 4\%$ for $Re = 14000$.

5. Discussion

5.1. *Physical mechanism*

To understand why end-plates create meridional flow, consider the transport equation for the azimuthal vorticity $\zeta := \partial_z u - \partial_r w$. For the axisymmetric and steady base flow, this equation can be written as

$$\left[\left(U\partial_r + W\partial_z - \frac{U}{r} \right) - \frac{1}{Re} \left(\nabla^2 - \frac{1}{r^2} \right) \right] \zeta_B = \partial_z \left(\frac{V^2}{r} \right) + Ri_g \partial_r \rho_B \qquad (5.1)$$

In the absence of end-plates and stratification, the right-hand side of (5.1) is exactly zero, and the basic flow solution satisfies $\zeta_B = 0$ which implies that there is no meridional flow. In this case, the cyclostrophic balance $V^2/r = \mathrm{d}P/\mathrm{d}r$ is satisfied everywhere in the flow. When end-plates are added, the boundary condition on the azimuthal velocity

disrupts this equilibrium (Czarny *et al.* 2003) and a now non-vanishing torque term $\partial_z \left(V^2/r \right) \neq 0$ (due to an inhomogeneous centrifugal force along z) generates meridional vorticity. When stratification is added, the baroclinic torque $Ri_g \partial_r \rho_B$ counteracts this effect, leaving the flow virtually free of meridional vorticity when the right-hand side becomes negligible. If we estimate that $r \approx 1/2(r_i^\star + r_o^\star) = 1/2(1+\eta)/(1-\eta)$, $V \approx 1$ and $\partial_z = O\left(d/(l/2)\right) = O\left(2/(\alpha\Gamma)\right)$, this occurs for

$$Ri_l \approx \frac{4\eta^2}{(\alpha\Gamma)^2(1-\eta^2)\partial_r\rho_B}. \tag{5.2}$$

This expression confirms that thick layers, i.e. large $\alpha\Gamma$, are more efficient at suppressing meridional motion, as they require a lower value of Ri_l. There are indeed two reasons to try and minimize the required value for Ri_l in experiments. Firstly, $Ri_l \propto \Omega_i^{-2}$ decreases rapidly with increasing $Re \propto \Omega_i$ at fixed buoyancy frequency N. Secondly, the maximum buoyancy frequency N is set by saturation of salt into water at $\Delta\rho/\rho_0 \approx 20\%$, limiting in turn the maximum $Ri_l \propto N^2 \propto \Delta\rho/\rho_0$. Therefore, thick layers are helpful when trying to maximise Re in an experiment while satisfying (5.2). As discussed in §4.3, this only remains true as long as the aspect ratio of the unstratified zone $\Gamma(1-\alpha)$ does not become small.

By estimating an upper bound for $\partial_r\rho_B$, it is also possible to evaluate a lower bound for Ri_l. Looking at the density field in figure 9, we observe that the isopycnals are approximately straight lines in the meridional plane, except at the inner corners. In dimensional units, the radial density gradient must therefore be lower than $\Delta\rho/(2d)$, since, by definition, the initial density jump across one layer is equal to $\Delta\rho/2$. This leads to the nondimensional estimate $\partial_r\rho < 1/2$. For $\alpha = 0.5$, $\eta = 0.417$ and $\Gamma = 3$, we obtain the upper bound $Ri_l > 0.75$, which is consistent with the observation that $\Delta_\perp$ is nearly constant beyond that value in figure 8.

Finally, we note that in the case of Dirichlet boundary conditions on the density, the baroclinic term is infinitesimally small in the vicinity of the end-plates, making it impossible to fully cancel the centrifugal torque term. This centrifugal torque is large in the vicinity of the inner corners because of the sharp vertical variation in V, explaining the locally higher levels of $\|\mathbf{U}_\perp\|$.

5.2. *Effect of Prandtl number*

Figure 12 shows the impact of the Prandtl number on the deviations Δ_V and $\Delta_\perp$ defined in (4.1). It appears that larger Pr leads to a significant reduction in both quantities, following approximate power laws $\Delta_V \propto Pr^{-0.47}$ and $\Delta_\perp \propto Pr^{-0.7}$ in the range $Pr \in [1, 46]$ for $Re = 5000$. This behaviour suggests that stratification with salt ($Sc \approx 700$) ought to be more efficient than stratification with temperature ($Pr \approx 7$), ignoring the differing boundary conditions. This observation suggests that our numerical model overestimates the departure of the experiment from (1.1), as can also be seen in figure 11. This results reinforces our confidence in the effectiveness of our method.

5.3. *Effect of no-flux boundary conditions on density*

Aside from the difference in Reynolds numbers, the only remaining discrepancy between the model and the experiment lies in the boundary conditions for the density. In our model, we assumed that stratification was permanently forced by applying a temperature profile at the walls, whereas in the experiments, the density is only controlled at $t = 0$. In the experiment, a piecewise linear density profile of the form (2.11) is set initially, but it is subject to no-flux boundary conditions $\partial_n\rho_B$ at all times. Because of mass diffusion, the only possible steady state solution is unfortunately unstratified. Yet, given
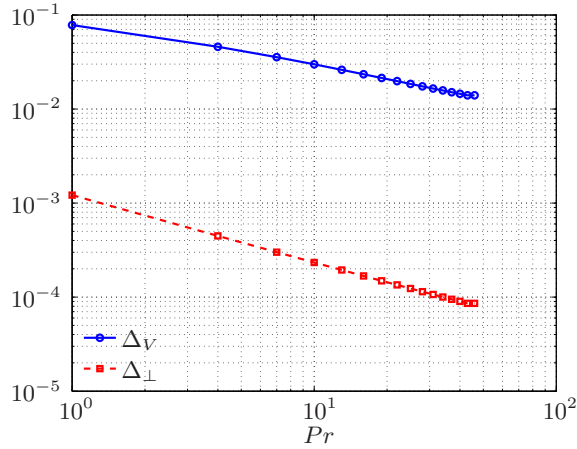
FIGURE 12. Effect of the Prandtl number on the deviations Δ_V and $\Delta_\perp$ for the HS case $\mu = \eta^{3/2}$, $\alpha = 0.5$ and $Ri_l = 2$.

the large value of the Schmidt number $Sc = \nu/\kappa \approx 700$ in the experiment, there is a separation of time scales between momentum diffusion $\tau_\nu = d^2/\nu$ and mass diffusion $\tau_\kappa = d^2/\kappa$ which translates into a quasi-steady evolution of the flow after a few units of τ_ν. But simulating such large Sc number flows proves computationally expensive as the corresponding separation of length scales is also large. Indeed, if we estimate the smallest inhomogeneity scale in the flow to be given by the Batchelor (1959) scale (formally defined for a stratified turbulent flow) $L_B \sim Sc^{-1/2}$ (or $L_B \sim Pr^{-1/2}$ for temperature), we expect it to be one order of magnitude smaller for $Sc = 700$ than for $Pr = 7$. The resulting increase in computational cost did not allow us to perform the calculations in a reasonable timeframe with the present codes.

However, it is in principle possible to satisfy the separation of time scales $\tau_\kappa/\tau_\nu = Sc \gg 1$ without taking Sc as large as 700. One might hope that a lower value of Sc, for instance $Sc = 30$, would suffice. Figure 13 shows that this is not the case. Indeed, the discontinuity of V in the corners leads to local overturning of the density field, hence strongly curved isopycnals (see figure 9). As a result, the mass diffusion term in equation (2.6d) is not negligible in these corners, despite the small prefactor $(Re\,Sc)^{-1} \approx 7 \times 10^{-6}$. Therefore, the rate of expansion of the meridional circulation cannot be approximated by τ_κ^{-1}, as the inhomogeneity length scale in the corners is much smaller than d. We conclude that it is not possible to compute quasi-steady solutions even for Schmidt numbers in the range $1 \ll Sc \ll 700$. This prohibits the use of linear stability analysis and motivates the use of Dirichlet (temperature) boundary conditions in our model.

Despite an inadequate separation of time scales, it is worth noting that the aspect of the solution at the inner corners in the initial stages of our simulation with Neumann (salt) boundary conditions (see figure 13(a) for $t = 0.5\tau_\nu$) is quite similar to the equivalent steady flow in figure 3(1b). This observation strengthens our confidence in the ability of the model with Dirichlet boundary conditions to capture the dynamics of the experiment.

5.4. *Seeking subcritical transition to turbulence*

After demonstrating that the parameter combination $(\ln \mu/\ln \eta, \alpha, Ri_l) = (0.5, 0.5, 2)$ satisfies all the constraints set forth in the introduction, we probed the possibility of sustained turbulence in the unstratified zone by carrying out a series of experiments.

In our first experiment, the flow was perturbed impulsively by reducing the inner
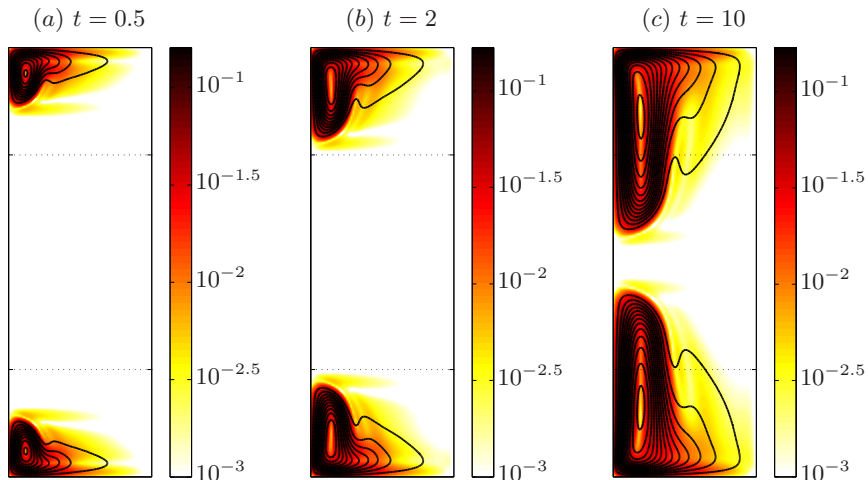
(a) $t = 0.5$ (b) $t = 2$ (c) $t = 10$

FIGURE 13. Meridional flow in the case of no-flux boundary conditions on density; HS case, $Re = 1000$, $\alpha = 0.5$, $Ri_l = 2$ and $Sc = 30$. The unit of time here is the density diffusion time $\tau_\nu = d^2/\nu$. Despite a large Schmidt number, there is no separation of time scales between diffusion of momentum and diffusion of density, leading to a rapid expansion of the meridional circulation. Contours and colourmap: same as figure 3(1) (here $\Delta\psi = 10^{-3}$). Dotted lines indicate the limit of the stratified layers at $t = 0$.

cylinder rotation rate by 75% in about 1s. A first PIV measurement was taken then (defining $t = 0$), before Ω_i was ramped back up to its final value over the course of 1 minute (approximately 10 inner cylinder rotation periods). A second measurement was made 30 minutes later, at $t \approx \tau_\nu/10$. Figure 14 shows the deviation from the unperturbed state $\mathbf{q}_\infty$ (time-averaged azimuthal profile $\overline{v}_\infty$ shown in figure 11), measured by $\Delta_\infty := \sqrt{\overline{u^2 + (v - \overline{v}_\infty)^2}}/\overline{v}_\infty$, at both instants. At $t = 0$ (dashed line), the perturbation extends radially over a distance $d' \approx d/10$, corresponding to an effective diffusion time $\tau'_\nu = d'^2/\nu \approx \tau_\nu/100$. At $t \approx \tau_\nu/10 \approx 10\tau'_\nu$ (solid line), the perturbation has completely diffused and the flow has relaxed to its unperturbed laminar state, as indicated by the low value of $\Delta_\infty \approx 1\%$ over the entire radial range.

In addition to that, we also tried to trigger subcritical transition to turbulence using two types of non-axisymmetric perturbations. After the spin-up procedure, a turbulent radial jet was introduced at the equator using a syringe and a needle of diameter 1 mm. The needle was introduced into the flow through a hole in the top end-plate before passing through the upper stratified region to reach the unstratified core. No discernible mixing was introduced in the stratified region throughout this procedure. The perturbation velocity in the jet was approximately 7% fo the inner cylinder velocity, but sustained turbulence was not triggered, with the flow relaminarising within 30 minutes. The second non-axisymmetric perturbation involved the same needle set-up but this time fluid was removed from the unstratified core region to induce vortex stretching. Once again, no sustainable turbulence was generated using this method.

All these observations show the robustness of the laminar flow with respect to finite-amplitude perturbations, and indicate its nonlinear stability at $Re = O(10^4)$ and $\mu = \eta^{1/2}$. This conclusion is consistent with recent numerical and experimental results by Ostilla-Mónico *et al.* (2014) and Edlund & Ji (2014), at even higher Reynolds number and larger rotation ratios. The first authors used axially periodic direct numerical simulation (with no stratification), and could not find any evidence of self-sustaining process up to
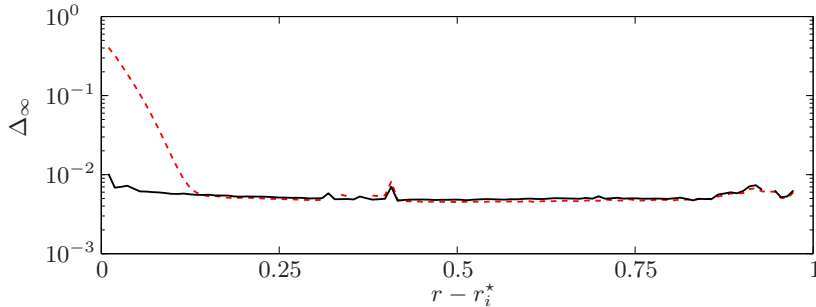
FIGURE 14. Deviation Δ_∞ from the unperturbed state at the equator when searching for sub-critical transition to turbulence. The dashed curve shows a measure of Δ_∞ right after applying the pertubation and the solid line corresponds to the deviation 30 min later. For this forcing at $Re = O(10^4)$, turbulence is not triggered in the unstratified zone as is evident from the low values of $\Delta_\infty \approx 1\%$ rapidly reached.

$Re = O(10^5)$ with $\mu = \eta^{3/2}$. Similarly, the latter authors, from the Princeton group, found robust decay of various types of initial perturbations in their enhanced split-ring apparatus (HTX device) at Re even greater than 10^6, with $\mu = \eta^{1.8}$.

6. Conclusions

In this work we have confirmed both experimentally and numerically the severe effect end-plates have on the interior of Taylor–Couette flow in the quasi-Keplerian regime. In the 'high-shear case' $\mu = \eta^{3/2}$, two symmetric recirculation cells are generated in the meridional plane; these merge at the equator to form a strong radial jet. This jet re-distributes angular momentum, causing the flow to become turbulent through a linear instability. In the 'low-shear case' $\mu = \eta^{1/2}$, the meridional flow is weaker, and there is no radial jet at the equator for the same value of Re. Despite remaining approximately invariant along the axial direction, the azimuthal flow is however significantly disturbed by the presence of end-plates and deviates from the 'ideal' Taylor–Couette solution corresponding to an axially-unbounded system.

We have then examined how stable stratification can be judiciously used to mitigate these end-effects in order to recover 'ideal' Taylor–Couette flow. When stratification is added across the full height, axisymmetric meridional flow is only able to develop in boundary layers near the end-plates and recirculation becomes essentially confined to the inner corners, where the azimuthal velocity is discontinuous. Everywhere else in the flow, the deviation with respect to the ideal velocity profile drops significantly. The physical mechanism behind this passive control method is the competition between the 'centrifugal' torque term $\partial_z(v^2/r)$ responsible for the generation of azimuthal vorticity, and the baroclinic torque $Ri_g\partial_r\rho$ acting against it. This mechanism is robust enough that similar enhancement of the base flow in the equatorial region can be achieved even when stratification is restricted to layers adjacent to the top and bottom end-plates. As long as the stable stratification is strong enough, typically $1 < Ri_l < 5$, and that neither the stratified nor the unstratified layers are too shallow (typically $\alpha \approx 0.5$ for $\Gamma = 3$), the control of the base flow is effective.

One obvious advantage of the approach is that it is much easier to implement than complex designs such as split-endcaps (Ji *et al.* 2006; Edlund & Ji 2014) or split inner cylinder (Paoletti & Lathrop 2011). By simply adding salt in varying concentration to the

working fluid, we managed to significantly mitigate end-effects and recover the Couette flow solution around the equator $z = 0$.

However, like any other control method, this approach has its limits. Firstly, the method is only applicable to rotation ratios in the range $\eta \lesssim \mu < 1$, corresponding to the least-sheared configurations in the quasi-Keplerian range $\eta^2 < \mu < 1$. When $\mu < \eta$, the stratorotational instability develops in the stratified layers, despite the presence of the unstratified region and end-plates. This instability destroys the initial density profile, rendering the method ineffective. Secondly, applying the method at very high Reynolds number, of the order of 10^6 or more, is challenging due to the eventual saturation of water by salt. For example, taking $Ri_l = 2$, $\Delta\rho/\rho_0 \approx 20\%$ (saturation threshold for salt in water) and a layer height of 0.75 gap (corresponding to $\alpha\Gamma = 1.5$ as in §4.3), means that reaching $Re = 10^6$ would require a huge tank of outer radius $r_o \approx 2\,\mathrm{m}$ or more.

This aside, we have successfully demonstrated the applicability of the method at $Re = O(10^4)$ for the rotation ratio $\mu = \eta^{1/2}$, and found turbulence decay following several types of large-amplitude disturbances. This result is consistent with the most recent numerical (Ostilla-Mónico *et al.* 2014) and experimental (Edlund & Ji 2014) investigations at respectively $Re = O(10^5)$ and $Re = O(10^6)$, hence further strengthens the view that extra physics beyond that of a simple rotating shear flow is needed to explain the inferred turbulence in weakly ionized accretion disks (see Turner *et al.* (2014) for a recent review of other possible instability mechanisms).

Acknowledgements

REFERENCES

ABSHAGEN, J., HEISE, M., PFISTER, G. & MULLIN, T. 2010 Multiple localized states in centrifugally stable rotating flow. *Phys. Fluids* **22**, 021702.

AVILA, M. 2012 Stability and angular-momentum transport of fluid flows between corotating cylinders. *Phys. Rev. Lett.* **108**, 124501.

AVILA, M., GRIMES, M., LOPEZ, J. M. & MARQUES, F. 2008 Global endwall effects on centrifugally stable flows. *Phys. Fluids* **20**, 104104.

BALBUS, S. A. 2011 Fluid dynamics: a turbulent matter. *Nature* **470**, 475–476.

BALBUS, S. A. & HAWLEY, J. F. 1991 A powerful local shear instability in weakly magnetized disks.1. linear analysis. *Ap. J.* **376**, 214–222.

BALBUS, S. A. & HAWLEY, J. F. 1998 Instability, turbulence and enhanced transport in accretion disks. *Rev. Mod. Phys.* **70**, 1–53.

BATCHELOR, G. K. 1959 Small-scale variation of convected quantities like temperature in turbulent fluid. part 1. general discussion and the case of small conductivity. *J. Fluid Mech.* **5**, 113–133.

CHANDRASEKHAR, S. 1960 The stability of non-dissipative couette flow in hydromagnetics. *Proc. Natl. Acad. Sci.* **46**, 253–257.

CZARNY, O., SERRE, E., BONTOUX, P. & LUEPTOW, R. M. 2003 Interaction between Ekman pumping and the centrifugal instability in Taylor–Couette flow. *Phys. Fluids* **15**, 467–477.

DALZIEL, S. B., CARR, M., SVEEN, J. K. & DAVIES, P. A. 2007 Simultaneous synthetic Schlieren and PIV measurements for internal solitary waves. *Meas. Sci. Tech.* **18**, 533–547.

DUBRULLE, B., MARIÉ, L., NORMAND, C., RICHARD, D., HERSANT, F. & ZAHN, J.-P. 2005 A hydrodynamic shear instability in stratified disks. *A & A* **429**, 1–13.

EDLUND, E. M. & JI, H. 2014 Nonlinear stability of laboratory quasi-Keplerian flows. *Phys. Rev. E* **89**, 021004.

HOLLERBACH, R. & FOURNIER, A. 2004 End-effects in rapidly rotating cylindrical Taylor–Couette flow. In *MHD Couette Flows: Experiments and Models*, , vol. 733, pp. 114–121.

JI, H., BURIN, M., SCHARTMAN, E. & GOODMAN, J. 2006 Hydrodynamic turbulence cannot transport angular momentum effectively in astrophysical disks. *Nature* **444**, 343–346.

LE BARS, M. & LE GAL, P. 2007 Experimental analysis of the stratorotational instability in a cylindrical Couette flow. *Phys. Rev. Lett.* **99** (6), 064502.

LE DIZÈS, S. & RIEDINGER, X. 2010 The strato-rotational instability of Taylor–Couette and Keplerian flows. *J. Fluid Mech.* **660**, 147–161.

LECLERCQ, C., PIER, B. & SCOTT, J. F. 2013 Temporal stability of eccentric Taylor–Couette–Poiseuille flow. *J. Fluid Mech.* **733**, 68–99.

LOPEZ, J. M., MARQUES, F. & AVILA, M. 2013 The Boussinesq approximation in rapidly rotating flows. *J. Fluid Mech.* **737**, 56–77.

LOPEZ, J. M. & SHEN, J. 1998 An efficient spectral-projection method for the Navier–Stokes equations in cylindrical geometries: I. axisymmetric cases. *J. Comp. Phys.* **139**, 308–326.

MOLEMAKER, M. J., MCWILLIAMS, J. C. & YAVNEH, I. 2001 Instability and equilibration of centrifugally stable stratified Taylor–Couette flow. *Phys. Rev. Lett.* **86**, 5270.

OSTILLA-MÓNICO, R., VERZICCO, R., GROSSMANN, S. & LOHSE, D. 2014 Turbulence decay towards the linearly stable regime of Taylor–Couette flow. *J. Fluid Mech.* **748**, R3.

PAOLETTI, M. S. & LATHROP, D. P. 2011 Angular momentum transport in turbulent flow between independently rotating cylinders. *Phys. Rev. Lett.* **106**, 024501.

PEYRET, R. 2002 *Spectral methods for incompressible viscous flow*. Springer.

RAYLEIGH, L. 1917 On the dynamics of revolving fluids. *Proc. R. Soc. Lond.* A *Mat.* **93**, 148–154.

RICHARD, D. & ZAHN, J.-P. 1999 Turbulence in differentially rotating flows. *A & A* **347**, 734–738.

RÜDIGER, G. & SHALYBKOV, D. A. 2009 Stratorotational instability in MHD Taylor–Couette flows. *A & A* **493**, 375–383.

SHALYBKOV, D. & RÜDIGER, G. 2005 Stability of density-stratified viscous Taylor–Couette flows. *A & A* **438** (2), 411–417.

TURNER, N. J., S., FROMANG, C., GAMMIE, H., KLAHR, G., LESUR, M., WARDLE & X.-N., BAI 2014 *Transport and accretion in planet-forming disks*. University of Arizona Press.

VELIKHOV, E. P. 1959 Stability of an ideally conducting liquid flowing between cylinders rotating in a magnetic field. *J. Exptl. Theoret. Phys.* **36**, 1398–1404.

YAVNEH, I., MCWILLIAMS, J. C. & MOLEMAKER, M. J. 2001 Non-axisymmetric instability of centrifugally stable stratified Taylor–Couette flow. *J. Fluid Mech.* **448**, 1–21.

ZELDOVICH, Y. B. 1981 On the friction of fluids between rotating cylinders. In *P. Roy. Soc. Lond. A Mat.*, , vol. 374, pp. 299–312.